

## MODELING THE HIGH-ENERGY EMISSION IN GRB 110721A AND IMPLICATIONS ON THE EARLY MULTIWAVELENGTH AND POLARIMETRIC OBSERVATIONS

N. FRAIJA<sup>1†</sup>, W. H. LEE<sup>1</sup>, M. ARAYA<sup>2</sup>, P. VERES<sup>3</sup>, R. BARNIOL DURAN<sup>4</sup> AND S. GUIRIEC<sup>5,6</sup>

<sup>1</sup> Instituto de Astronomía, Universidad Nacional Autónoma de México, Circuito Exterior, C.U., A. Postal 70-264, 04510 Cd. de México, México.

<sup>2</sup> Escuela de Física & Centro de Investigaciones Espaciales (CINESPA), Universidad de Costa Rica, San José 2060, Costa Rica

<sup>3</sup> Center for Space Plasma and Aeronomic Research (CSPAR), University of Alabama in Huntsville, Huntsville, AL 35899, USA

<sup>4</sup> Department of Physics and Astronomy, California State University, Sacramento, 6000 J Street, Sacramento, CA 95819-6041, USA

<sup>5</sup> Department of Physics, The George Washington University, 725 21st Street NW, Washington, DC 20052, USA

<sup>6</sup> NASA Goddard Space Flight Center, Greenbelt, MD 20771, USA

*Draft version July 5, 2021*

### ABSTRACT

GRB 110721A was detected by the Gamma-ray Burst Monitor and the Large Area Telescope (LAT) onboard the Fermi satellite and the Gamma-ray Burst Polarimeter onboard the IKAROS solar mission. Previous analysis done of this burst showed: i) a linear polarization signal with position angle stable ( $\phi_p = 160^\circ \pm 11$ ) and high degree of  $\Pi = 84_{-28}^{+16}$  %, ii) an extreme peak energy of a record-breaking at  $15 \pm 2$  MeV, and iii) a subdominant prompt thermal component observed right after the onset of this burst. In this paper, the LAT data around the reported position of GRB 110721A are analysed with the most recent software and then, the LAT light curve above 100 MeV was obtained. The LAT light curve is modelled in terms of adiabatic early-afterglow external shocks when the outflow propagates into a stellar wind. Additionally, we discuss the possible origins and also study the implications of the early-afterglow external shocks on the extreme peak energy observed at  $15 \pm 2$  MeV, the polarization observations and the subdominant prompt thermal component.

*Subject headings:* gamma-rays bursts: individual (GRB 110721A) — Physical data and processes: acceleration of particles — Physical data and processes: radiation mechanism: nonthermal

### 1. INTRODUCTION

Magnetic field plays an important role in the gamma-ray burst (GRB) physics of relativistic jets (i.e. in their formation, collimation and acceleration, Blandford & Znajek 1977; Komissarov 2001; Tchekhovskoy et al. 2010; Tchekhovskoy 2015; Bromberg & Tchekhovskoy 2016). Our understanding of magnetic field properties in the GRB scenery has swiftly increased through the last years due to observational success of polarimetry from prompt and/or early afterglow emission (Götz et al. 2009; Yonetoku et al. 2012; Mundell et al. 2007; Steele et al. 2009; Kopač et al. 2015; Pruzhinskaya et al. 2014; Gorbvskoy et al. 2016). Simulations of magneto-hydrodynamic (MHD) flows have revealed that internal shocks can hardly describe the polarization degree larger than 30 percent (Inoue et al. 2011). A high polarization degree is difficult to reconcile without a magnetic field that is ordered on large scales (e.g. external reverse shocks, Granot et al. 2015). The polarization properties found in some GRBs have shown that outflows can be strongly magnetized and large-scale uniform fields can also survive long after the initial explosion (Mundell et al. 2013; Coburn & Boggs 2003; Rutledge & Fox 2004). Additionally, the values of the magnetic energy density in the reverse-shock region found to be higher than in the forward-shock region have claimed that GRBs are magnetised (Zhang & Kobayashi 2005; Zhang et al. 2003; Kobayashi et al. 2007; Sacahui et al. 2012; Fan et al. 2004; Fraija et al. 2012; Fraija 2015; Fraija et al. 2017). GRB 110721A was detected by the Gamma-ray Burst Monitor (GBM) and Large Area Telescope (LAT) onboard Fermi Gamma-ray Space Telescope. At 04:47:43.75 UT, 2011 July 21, Fermi-GBM triggered on GRB 110721A (Tierney & von Kienlin 2011) and immediately at 04:47:45, LAT detected high-energy emission from GRB 110721A

(Vasileiou et al. 2011). This burst had an initial peak energy of a record-breaking  $15 \pm 2$  MeV and a subdominant prompt thermal component, observed right after the onset of the burst (Axelsson & et al. 2012). The evolution in time of the extreme peak energy was modeled with a power-law function and the thermal component with a blackbody spectrum. In the photospheric and internal shock scenarios, many authors have discussed the origin of both the subdominant prompt thermal component (Iyyani et al. 2016; Ahlgren et al. 2015; Pe'er et al. 2015; Bégué & Pe'er 2015; Lundman et al. 2013) and the brightest peak (Zhang et al. 2012; Veres et al. 2012) present in GRB 110721A. In particular, Zhang et al. (2012) and Veres et al. (2012) showed that the brightest peak at 15 MeV cannot be explained in terms of the standard internal shocks scenario but possibly through the dissipative photospheric synchrotron models in a magnetically-dominated outflow. Zhang et al. (2012) proposed that the rapid "hard-to-soft" spectral evolution was consistent with a quick discharge of magnetic energy in a magnetically-dominated outflow. Using the Gamma-ray Burst Polarimeter (GAP) onboard IKAROS solar sail mission, Yonetoku et al. (2012) reported polarization measurements in the onset of this burst. Based on the early measurements done on the polarization degree and position angle, authors suggested that synchrotron emission model was more consistent than photospheric quasi-thermal emission models.

In this work, the LAT light curve is obtained and then, it is modelled using the early-afterglow external shock model previously described in Fraija (2015) and Fraija et al. (2016a). In addition, the implications of the early-afterglow external shocks on the extreme peak energy observed at 15 MeV, the polarization observations and the subdominant prompt thermal component were studied and also discussed. The paper is arranged as follows: in Section 2 a brief description

of the multiwavelength and polarimetric observations is given, and also the results on the analysis of the LAT data are presented. In Section 3, a successful description of the LAT emission is presented in the context of the early-afterglow external shock model. In Section 4 we study and discuss the implications of the early-afterglow external shock on the early multiwavelength and polarimetric observations, and brief conclusions are given in Section 5.

## 2. GRB 110721A

### 2.1. Multiwavelength observations

GRB 110721A exhibited a complex spectral and temporal behaviour, similar to LAT bursts observed by Fermi. This burst had an initial off-axis angle around  $\sim 40^\circ$  in the LAT and the autonomous repointed request triggered by the GBM brought it down to  $\sim 10^\circ$  (Ackermann et al. 2013). GRB 110721A triggered the GBM instrument at 04:47:43.75 UT on 2011 July 21 (Tierney & von Kienlin 2011). Immediately, LAT started detecting high-energy emission since 04:47:45 UT up to more than 200 s (Vasileiou et al. 2011). Using a standard event selection, LAT observed 20 photons above 100 MeV. The most energetic photon with energy of  $6.3 \pm 0.6$  GeV was detected at 4.5 s after the initial trigger. The light curve of LAT Low Energy (LATLLE) events displayed a typical short emission component at early onset. This short component which lasted much less than the prompt emission, presented photons between 30 - 130 MeV (Axelsson & et al. 2012). The main emission lasting  $T_{90} = 24.5$  s in the GBM, consisted of one considerable episode with a peak flux of  $5.7 \pm 0.2 \times 10^{-5}$  erg cm $^{-2}$  s $^{-1}$ . In addition, GRB 110721A exhibited right after the onset a subdominant prompt thermal component peaking at  $\sim 80$  keV and an extreme peak energy ever detected in a burst of  $15 \pm 2$  MeV (Axelsson & et al. 2012).

From 1840 s to 26 hrs after the trigger, this burst was observed by the Swift X-ray Telescope (XRT). Greiner et al. (2011) and Grupe et al. (2011) found a faint X-ray emission from the location of this burst. The Gamma-Ray Burst Optical/Near-Infrared Detector (GROND; Greiner et al. 2011) and also for more than 3000 sec Gemini Multi-Object Spectrographs (GMOS; Berger 2011) detected its optical counterpart and measured two redshifts:  $z=0.382$  from the absorption lines of CaII and  $z=3.512^1$  from Ly-alpha absorption.

IKAROS-GAP detected a linear polarization signal with position angle stable ( $\phi_p = 160^\circ \pm 11$ ) and high degree of  $\Pi = 84_{-28}^{+16}$  %.

### 2.2. LAT data analysis

Event data files were obtained starting at a few seconds before the GBM trigger time for GRB 110721A, 04:47:43 UT on 2011 July 21 (Ackermann et al. 2013). Fermi-LAT data above 100 MeV are reduced using the public database at the Fermi Web site<sup>2</sup>. These data are analysed with the most recent software SCIENCETOOLS version v10r0p5<sup>3</sup> and reprocessed with ‘‘Pass 8’’ extended, spacecraft data and the instrument response functions P8R2\_TRANSIENT020\_V6. Transient events are selected within  $15^\circ$  of the reported position of the GRB

above an energy of 100 MeV with a maximum zenith angle of  $100^\circ$ . Using the `gtfindsrc` Fermi Science tool<sup>4</sup> with data obtained within 30 s of the trigger time, the position of the event is found to be at the coordinates (J2000)  $\alpha = 333^\circ.52$ ,  $\delta = -38^\circ.60$ , with an error circle of radius  $0.09^\circ$ .

Exposure maps are generated with the tool `gtexppmap` Fermi Science tool, and standard spectra and response files with the `gtbin` and `gtspgen` Fermi Science tools for analysis with the software XSPEC version 12 (Arnaud 1996). No other sources in the LAT catalog or background emission are considered due to the duration of the event. Data from 0.025 s to the first second after trigger is binned in three logarithmically-spaced time bins and the spectra are fitted with a power-law in each bin. The spectral index is kept frozen to the value obtained for the analysis of the joint data within this time period, 2.6 s. The resulting fluxes with  $1\sigma$  errors in each time bin are calculated after the fit, and then the light curve with the flux above 100 MeV is shown in Figure 1 (left panel). The LAT light curve exhibits a peak at  $\sim 0.3$  s similar to the peak displayed in the LATLLE light curve between 30 - 130 MeV (Axelsson & et al. 2012).

## 3. MODELING THE LAT LIGHT CURVE

LAT light curve of GRB 110721A presented in Figure 1 (left) is similar to the LAT-detected bursts such as GRB090510 (Ackermann & et al. 2010; He et al. 2011), GRB 110731A (Ackermann & et al. 2013), GRB 130427A (Ackermann et al. 2014) among other powerful bursts. It has been extensively claimed that GeV photons in the prompt emission could be of early-afterglow external origin (e.g. see Kumar & Barniol Duran 2009, 2010; Ghisellini et al. 2010; Fraija 2015; Fraija et al. 2016b). In order to describe the LAT light curve displayed in Section 2, we require the observable quantities of GRB 110721A for the two redshifts  $z=0.382$  and  $z=3.512$  (Berger 2011), and use the early-afterglow external shock model presented in Fraija (2015) and Fraija et al. (2016a). We identify two emission components, one component lasting less than a few of seconds (the so-called short-lived component; see, e.g., Fan et al. 2004; Zhang & Kobayashi 2005; Fraija et al. 2012) and other component lasting more than hundred of seconds (the so-called long-lived component; see e.g. Kumar & Barniol Duran 2009, 2010; Ghisellini et al. 2010; He et al. 2011; Fraija et al. 2016b). We hereafter use  $k=h=c=1$  in natural units, and the values of cosmological parameters  $H_0 = 71$  km s $^{-1}$  Mpc $^{-1}$ ,  $\Omega_m = 0.27$ ,  $\Omega_\lambda = 0.73$  (Spergel et al. 2003). The values of bulk Lorentz factor  $\Gamma$  is constrained through the deceleration time  $t_{\text{dec}} = 9/(64\pi)(1+z)\xi^{-2}EA^{-1}\Gamma^{-4}$ , where  $A$  is the stellar wind density,  $\xi$  is a parameter of the order of unity and  $E = E_{\gamma,iso}/\eta$  is the isotropic equivalent kinetic energy with  $\eta \approx 0.2$  the kinetic efficiency to convert bulk kinetic energy to  $\gamma$ -ray energy  $E_{\gamma,iso} \simeq 10^{54}$  erg for  $z=3.512$ . Taking into account the fact that the largest flux density (see the peak flux in fig.1) was present at  $\sim (0.25 - 0.35)$  s, and using the typical values of the electron power index  $p = 2.2$  and the stellar wind density  $A = A_*(5.0 \times 10^{11})$  g/cm with  $A_* = 0.1$  (Chevalier & Li 2000; Ackermann et al. 2014; Ackermann & et al. 2013; Fraija et al. 2016a; Fraija 2015), then the value of the bulk Lorentz factor was found to be  $\Gamma \simeq 1000$  and the corresponding deceleration radius becomes  $r_{\text{dec}} \simeq 9.9 \times 10^{15}$  cm. The value of the electron spectral index  $p = 2.2$  was estimated through the slope decays of the LAT long-lived component found  $\alpha_{LAT} = 1.13 \pm 0.11$  and

<sup>1</sup> This value is more consistent in accordance with the  $E_{p,i} - E_{\gamma,iso}$  correlation (Amati et al. 2008).

<sup>2</sup> <http://fermi.gsfc.nasa.gov/ssc/data>

<sup>3</sup> <http://fermi.gsfc.nasa.gov/ssc>

<sup>4</sup> <http://fermi.gsfc.nasa.gov/ssc/data/analysis>

the adiabatic synchrotron forward-shock emission in the fast cooling regime  $\frac{3p-2}{4}$ . The value of the Lorentz factor found is consistent with the thick-shell regime ( $\Gamma_c = 410 < \Gamma$ , with  $\Gamma_c$  the critical Lorentz factor; e.g. see Zhang & Kobayashi 2005; Zhang et al. 2003) for which the ejecta is essentially decelerated by the reverse shock. The shock crossing time is  $t_d \sim (\Gamma/\Gamma_c)^{-4} T_{90} \simeq 0.5$  s (Kobayashi & Zhang 2007) which is much shorter than the duration of the main burst and it is consistent with the duration of the short-lived component. It is worth noting that if we would have considered an homogeneous medium in stead of the stellar wind of the progenitor, the value of the bulk Lorentz factor at the initial deceleration phase of  $\sim (0.25 - 0.35)$  s would have been  $\simeq 2100$  for a typical constant density of  $n=1$  cm $^{-3}$  or  $\simeq 1000$  for  $n=300$  cm $^{-3}$  which in both cases the values are fairly high.

We did the Chi-square  $\chi^2$  minimization using the ROOT software package (Brun & Rademakers 1997) to fit the LAT light curve shown in fig.1 (left panel) and then, we obtain the values of microphysical parameters for  $\xi=0.75$ . The parameter  $\xi$  is a correction factor of the bulk Lorentz factor and the emitting radius due to these quantities are derived to be applied only in the line of sight to the center (Panaitescu & Mészáros 1998; Chevalier & Li 2000). Left panel in Figure 1 shows the contributions of synchrotron radiation from forward shock (dash-dotted line) and synchrotron self-Compton (SSC) emission from reverse shock (continuous line) that model the high-energy emission detected in GRB 110721A by the Fermi-LAT instrument, for  $z=0.382$  and  $z=3.512$ . The long-lived high-energy emission was interpreted by synchrotron radiation in the fast cooling regime for relativistic electrons radiating photons around 100 MeV at  $t=5$  s. The short-lived high-energy component was fitted with SSC emission from reverse shock in the thick-shell regime when the electron population radiates photons around 100 MeV at  $t=0.3$  s. The wind model predicts a rising of  $t^{1/2}$  (e.g., see Fraija et al. 2016a) and a steeper decline after the peak of  $t^{-5/2}$  (Kobayashi & Zhang 2003) or in some cases  $t^{-(p+4)/2}$  when the light curve is determined by the angular time delay effect (Kumar & Panaitescu 2000). It is worth noting that the solutions for the two redshifts are equal for different values of  $E_{\gamma, \text{iso}} = 1.4 \times 10^{52}$  erg and  $E_{\gamma, \text{iso}} = 1.2 \times 10^{54}$  erg for  $z=0.382$  and  $z=3.512$ , respectively, and sets of microphysical parameters ( $\epsilon_e$ ,  $\epsilon_{B,f}$  and  $\epsilon_{B,r}$ ), as shown in Figure 1 (right panel). This panel displays the values of microphysical parameters ( $\epsilon_e$ ,  $\epsilon_{B,f}$  and  $\epsilon_{B,r}$ ), for  $z=0.382$  and  $z=3.512$ , that reproduce the short- and long-lived LAT emissions. The subindexes “f” and “r” refer to quantities observed/derived in the forward- and reverse-shock regions, respectively. As indicated, the parameter space located at the left side in this figure explains the long-lived LAT flux through synchrotron emission from forward shock and at the right side describes the short-lived LAT flux by SSC from reverse shock. The values of the microphysical parameters in forward-shock region lie in the ranges of  $0.1 \leq \epsilon_e \leq 1.0$ ,  $4 \times 10^{-6} \leq \epsilon_{B,f} \leq 10^{-4}$  ( $3 \times 10^{-5} \leq \epsilon_{B,f} \leq 8 \times 10^{-4}$ ) for  $z=3.512$  (0.382) and in reverse-shock region lie in the ranges of  $0.1 \leq \epsilon_e \leq 0.74$  and  $0.32 \leq \epsilon_{B,r} \leq 0.5$  for  $z=0.382$  and  $0.1 \leq \epsilon_e \leq 0.82$  and  $0.25 \leq \epsilon_{B,r} \leq 0.35$  for  $z=3.512$ .

From the range obtained of  $\epsilon_{B,r}$ , the magnetization parameter lies in the range of  $0.32 \leq \sigma \leq 0.5$  and  $0.25 \leq \sigma \leq 0.35$  for  $z=0.382$  and  $z=3.512$ , respectively. The magnetic field derived in forward- and reverse-shock regions can be

observed that it is  $\simeq 50 - 200$  (20 - 100) times larger in the reverse-shock region than in the forward-shock region for  $z=0.382$  (3.512). The previous results ( $\sigma \lesssim 1$ ) indicate that the flow is moderately magnetized and then, a bright  $\gamma$ -ray flash is expected as presented in some Fermi-detected bursts such as GRB090510 (Ackermann & et al. 2010; He et al. 2011; Fraija et al. 2016b), GRB 110731A (Ackermann & et al. 2013; Fraija 2015), GRB 130427A (Ackermann et al. 2014; Fraija et al. 2016a). Otherwise, the reverse shock emission is expected to be weak or suppressed if  $\sigma \ll 1$  or  $\sigma \gg 1$ . Even, for a magnetization parameter  $\sigma \geq 1$ , the reverse shock emission decreases substantially.

The maximum synchrotron energy at 4.5 s predicts photons with energy of  $E_{\text{max},f}^{\text{syn}} \simeq 4.1$  GeV  $\left(\frac{1+z}{4.512}\right)^{-3/4} \xi_{-0.12}^{-1/2} E_{54.7}^{1/4} A_{x,-1}^{-1/4} t_{0.65}^{-1/4}$ , then the most energetic photon present of  $6.3 \pm 0.6$  GeV necessarily must be interpreted by SSC emission from forward shock as explained in some powerful bursts such as GRB 130427A (Fan et al. 2013; Fraija et al. 2016a), GRB 090926A (Veres & Mészáros 2012; Sacahui et al. 2012), GRB 09510 (Corsi et al. 2010; Fraija et al. 2016b), see also e.g. Beniamini et al. (2015) and references therein.

#### 4. IMPLICATIONS OF THE EARLY-AFTERGLOW EXTERNAL SHOCK MODEL ON THE EARLY MULTIWAVELENGTH AND POLARIMETRIC OBSERVATIONS

In this section we discuss the possible origins of the extreme peak energy detected at  $15 \pm 2$  MeV, the polarization observations and the subdominant prompt thermal component. In addition, we study the implications of the early-afterglow external shock model used to describe the LAT light curve (see subsection 2.2) on these early multiwavelength and polarimetric observations.

##### 4.1. The extreme peak energy at $15 \pm 2$ MeV

In the standard fireball model, inhomogeneities in the jet lead to internal shell collisions, higher shells ( $\Gamma_h$ ) catching slower shells ( $\Gamma_l$ ). The kinetic energy of ejecta is partially dissipated via these internal shocks (Rees & Meszaros 1994) which take place at a distance of  $r_j = 6 \times 10^{15}$  cm  $\Gamma_{\text{is},3}^2 t_{\nu,-1}$ , where  $t_\nu$  is the variability time scale of the central object and  $\Gamma_{\text{is}} \simeq \sqrt{\Gamma_h \Gamma_l}$  is the bulk Lorentz factor of the propagating internal shocks. These shocks are expected to be collisionless, so that particles may be accelerated. The kinetic energy density

$$U = \gamma_{\text{sh}} / (8\pi) \Gamma_{\text{is}}^{-6} L_j t_\nu^{-2}, \quad (1)$$

with  $\gamma_{\text{sh}} = \sqrt{\frac{\gamma_{\text{in}}}{2}}$  and  $L_j$  the isotropic equivalent kinetic luminosity is equipartitioned to accelerate particles  $\epsilon_e = U_e/U$  and to generate and/or amplify the magnetic field  $\epsilon_B = B^2 / (8\pi U)$  (Piran 2005) with  $B$  the comoving magnetic field given by

$$B \simeq \sqrt{\gamma_{\text{sh}} \epsilon_B} \Gamma_{\text{is}}^{-3} L_j^{1/2} t_\nu^{-1}. \quad (2)$$

Here,  $\gamma_{\text{in}}$  is the Lorentz factor of internal shock which is of order of a few. The typical synchrotron energy from internal shock of an electron with a “typical” Lorentz factor ( $\gamma_e$ ) is

$$E_{p,(\gamma_e)}^{\text{is}} = \frac{e}{m_e} (1+z)^{-1} \Gamma_{\text{is}} \gamma_e^2 B. \quad (3)$$

We consider a “typical” electron as one that has the average  $\gamma_e$  of the electrons distribution  $\langle \gamma_e \rangle = \frac{U_e}{m_e N_e}$  (Piran 1999).

This average value can be estimated in two different cases. In the first case, the energy density carried by electrons and the electron number density are (Piran 1999)

$$U_e = \epsilon_e U = \epsilon_e \gamma_{\text{sh}} N_p m_p \quad \text{and} \quad N_e \simeq N_p. \quad (4)$$

Hence, the average Lorentz factor is  $\langle \gamma_e \rangle = \frac{m_p}{m_e} \epsilon_e \gamma_{\text{sh}}$ . In the second case, the energy density carried by electrons and the electron number density are

$$U_e = \frac{m_e A_e}{(p-2)} \gamma_{e,\text{min}}^{-p+2} \quad \text{and} \quad N_e = \frac{m_e A_e}{(p-1)} \gamma_{e,\text{min}}^{-p+1}, \quad (5)$$

for  $p > 2$  and  $\gamma_{e,\text{min}} \ll \gamma_{e,\text{max}}$ . Therefore,  $\langle \gamma_e \rangle = \frac{p-1}{p-2} \gamma_{e,\text{min}}$ . Summing up both cases, the observed synchrotron energy becomes With the typical values, we have

$$E_{p,\langle \gamma_e \rangle}^{\text{is}} \simeq \begin{cases} 0.3 \text{ MeV} \epsilon_{e,-0.3}^2 \gamma_{\text{sh}}^2 \\ 1.4 \text{ MeV} \gamma_{e,\text{min},3}^2 \\ \times \left( \frac{4.512}{1+z} \right) \sqrt{\gamma_{\text{sh}} \epsilon_{B,-1}^{1/2} t_{\nu,-1}^{-1} \Gamma_{\text{is},3}^{-2} L_{j,52}^{1/2}}. \end{cases} \quad (6)$$

It is worth noting that if only a small fraction of the electrons  $N_{e,\text{fr}}$  are accelerated, the average Lorentz factor  $\langle \gamma_{e,\text{fr}} \rangle = \frac{U_e}{m_e N_{e,\text{fr}}}$  is larger than  $\langle \gamma_e \rangle$ , and then  $E_{p,\langle \gamma_{e,\text{fr}} \rangle}^{\text{is}} > E_{p,\langle \gamma_e \rangle}^{\text{is}}$  (for a recent discussion see e.g.; Beniamini & Piran 2013). Including pair formation, a different calculation indicates an upper limit

$$E_p^{\text{is}} \lesssim 0.5 \text{ MeV} \left( \frac{1+z}{4.512} \right)^{-1} L_{52}^{-1/5} \Gamma_{\text{is},3}^{4/3} t_{\nu,-1}^{1/6} \epsilon_B^{1/2} \epsilon_e^{4/3}, \quad (7)$$

which is more rigorous (Guetta et al. 2001). Previous analysis indicates that the peak energy can hardly reach values as high as 15 MeV. In addition, the extreme peak energy of the Band function at  $15 \pm 2$  MeV was measured during the first time bin (from -0.32 to 0.0 s) with a low-energy power law index of  $\alpha = -0.81 \pm 0.08$  and a high-energy index of  $\beta = -3.5_{-0.6}^{+0.4}$  (Axelsson & et al. 2012). They found that the extreme peak energy decreased monotonically following a power law of the form  $E_p = A_{pl}(t - t_0)^\delta$  with  $\delta = -1.22 \pm 0.13$  for  $t_0 = -0.46$  s and  $A_{pl}$  the proportionality constant. However, it has been believed that synchrotron spectrum produced by electrons accelerated in relativistic internal shocks is expected in the fast cooling regime with photon spectral index of  $\alpha = -1.5$  (Rybicki & Lightman 1986). It is worth noting that standard internal shocks take place at  $6 \times 10^{15}$  cm and the deceleration radius found in this work is  $\sim 10^{16}$  cm, then a temporal gap between extreme peak energy and the LAT emission would have been detected, contrary what is observed. Therefore, the standard internal shocks cannot straightforwardly explain the value of energy peak at  $15 \pm 2$  MeV, the power spectral index associated with the initial flux and the timescale observed between the extreme peak energy and the LAT emission described in the external shock framework.

Uhm & Zhang (2014) showed that considering the effect of adiabatic expansion of magnetic field, the photon index of  $\alpha = -0.8$  could be due to synchrotron radiation in the moderately fast cooling regime. They proposed that a minimum electron Lorentz factor of the order of  $10^5$  and a strength of the magnetic field in the range of 10 – 100 G must be presented in the shocks in order to reproduce the value of the photon spectral index of  $\alpha = -0.8$ . A feasible scenario to provide these parameter requirements could be the magnetic

dissipation models that use a large dissipation radius, such as the internal collision-induced magnetic reconnection and turbulence (ICMART) events (Zhang & Yan 2011). In the ICMART framework, the Band function is formed at large radii from the central engine, typically at  $10^{15} - 10^{16}$  cm. Electrons are accelerated by runaway release of the storage magnetic field energy either in the reconnection zones, or stochastically in the turbulent areas, which emit synchrotron photons that power the prompt emission. During the ICMART event the magnetization parameter decreases fast. Initially, the magnetization parameter is the order of  $\sigma \simeq 100$ , and the discharge process ends when the microphysical parameter is reduced to  $\sigma \lesssim 1$ .

Taking into consideration the two timescales: the initial time  $t_0 = -0.46$  of the extreme peak energy at  $15 \pm 2$  MeV which must have begun before the first bin, (from -0.32 to 0; Axelsson & et al. 2012) and the deceleration time at  $\sim 0.3$  s used to describe the peak of the LAT emission, it is reasonable to infer that the prompt emission must have taken place at larger radius ( $10^{15} - 10^{16}$  cm) close to the deceleration radius  $\sim 10^{16}$ . On the other hand, the range of values of the magnetization parameters  $\sigma \sim 0.3 - 0.5$  obtained at the deceleration radius  $\sim 10^{16}$  cm encourage us to think that before deceleration, the ejecta must also have dissipated a significant amount of Poynting flux during the prompt emission phase. Therefore, from the analysis performed using the LAT emission can be seen that the most favorable mechanism to make this happen and explain in addition the photon index of  $\alpha = -0.8$  as synchrotron radiation in the cooling regime is the ICMART model.

#### 4.2. Polarization

Internal shocks may produce strong magnetic fields with random directions on hydrodynamic scales (Gruzinov & Waxman 1999; Inoue et al. 2011). MHD simulations with initial density fluctuations showed that internal shocks cannot explain the observed polarization degree of  $\Pi \gtrsim 30\%$  (Inoue et al. 2011). Such is the case of GRB 100826A, which exhibited gamma-ray polarization with polarization angle variable during the prompt emission and polarization degree of  $\Pi = 27 \pm 11\%$  (Yonetoku et al. 2011). Therefore, standard internal shocks could hardly explain the polarization percentage and the behavior of the polarization angle observed in GRB110721A. On the other hand, Yonetoku et al. (2012) showed that photospheric emission model cannot describe the polarization degree and the position angle observed in GRB110721A.

The detection of linear polarization in a few percent of GRB afterglows has been accepted as a real confirmation that the synchrotron radiation is the dominant emission mechanism in the afterglow phase. A high degree of linear polarization with a stable position angle is hard to produce without a magnetic field that is ordered on large scales (e.g. external reverse shocks, Granot et al. 2015). For instance, GRB 120308A was observed by the purpose-built RINGO2 polarimeter on the Liverpool Telescope (Virgili et al. 2012). RINGO2 observations started  $\sim 240$  s after the GBM trigger. Although the position angle remained almost stable, the polarization degree showed an evolution from  $\Pi = 28 \pm 4\%$  to  $\Pi = 16_{-4}^{+5}\%$  by 800 s after the GBM trigger (Mundell et al. 2013). The analysis performed by Mundell et al. (2013) shows that the polarization degree extrapolated to earlier times than  $\sim 300$  s, must be much higher than  $\Pi = 28\%$  as was found in GRB 110721A (Yonetoku et al. 2012), thus favouring the early afterglow emission. One of the implications of describing the LAT light curve

through the early afterglow emission is that the reverse shock could reproduce the high polarization degree (Granot & Königl 2003), as observed in this burst. It is worth noting that polarization percentage in the emission coming from shocked circumburst medium is expected to be very low (see e.g.; Covino et al. 1999; Greiner et al. 2003). Taking into account the energy range observed by IKAROS-GAP (70 - 300 keV), we will show that using the observable quantities of GRB 110721A and the microphysical parameter values found, the synchrotron reverse-shock flux at  $E^{\text{syn}} = 100$  keV dominates over that flux produced in the forward-shock region. The synchrotron spectral breaks (the characteristic  $E_m^{\text{syn}}$  and the cooling  $E_c^{\text{syn}}$  break energy) and the maximum synchrotron flux using  $z=3.512$ , for the forward and reverse shocks are (see e.g., Fraija 2015)

$$\begin{aligned} E_{m,f}^{\text{syn}} &\simeq 6.3 \text{ MeV} \left( \frac{1+z}{4.512} \right)^{1/2} \xi_{-0.12}^{-3} \epsilon_{e,-0.4}^2 \epsilon_{B,f,-5}^{1/2} E_{54.7}^{1/2} t_{-0.5}^{-3/2} \\ E_{c,f}^{\text{syn}} &\simeq 0.2 \text{ eV} \left( \frac{1+z}{4.512} \right)^{-3/2} \xi_{-0.12}^5 (1+x_f)^{-2} \epsilon_{B,f,-5}^{-3/2} \\ &\quad \times A_{\star,-1}^{-2} E_{54.7}^{1/2} t_{-0.5}^{1/2} \\ F_{\text{max},f}^{\text{syn}} &\simeq 3.8 \times 10^2 \text{ mJy} \left( \frac{1+z}{4.512} \right)^{3/2} \xi_{-0.12}^{-1} \epsilon_{B,f,-5}^{1/2} A_{\star,-1} D_{28.9}^{-2} \\ &\quad \times E_{54.7}^{1/2} t_{-0.5}^{-1/2}, \quad (8) \end{aligned}$$

and

$$\begin{aligned} E_{m,r}^{\text{syn}} &\simeq 0.2 \text{ keV} \left( \frac{1+z}{4.512} \right)^{-1/2} \xi_{-0.12}^{-1} \epsilon_{e,-0.4}^2 \epsilon_{B,r,-0.4}^{1/2} \Gamma_3^2 \\ &\quad \times A_{\star,-1} E_{54.7}^{-1/2} t_{d,-0.5}^{-1/2} \\ E_{c,r}^{\text{syn}} &\simeq 1.6 \times 10^{-5} \text{ eV} \left( \frac{1+z}{4.512} \right)^{-3/2} \xi_{-0.12}^5 (1+x_r)^{-2} \\ &\quad \times \epsilon_{B,r,-0.4}^{-3/2} A_{\star,-1}^{-2} E_{54.7}^{1/2} t_{d,-0.5}^{1/2} \\ F_{\text{max},r} &\simeq 1.7 \times 10^8 \text{ mJy} \left( \frac{1+z}{4.512} \right)^2 \xi_{-0.12}^{-2} \epsilon_{B,r,-0.4}^{1/2} \Gamma_3^{-1} A_{\star,-1}^{1/2} \\ &\quad \times D_{28.9}^{-2} E_{54.7} t_{d,-0.5}^{-1}, \quad (9) \end{aligned}$$

respectively, where  $x_{f/r}$  is the Compton parameter for the forward/reverse shocks. At  $E^{\text{syn}} = 100$  keV, the forward-shock synchrotron flux is in the energy range of  $E_{c,f}^{\text{syn}} < E^{\text{syn}} < E_{m,f}^{\text{syn}}$  (see eq. 8), and then it is given by  $F_{\nu,f} = F_{\text{max},f}^{\text{syn}} (E^{\text{syn}}/E_{c,f}^{\text{syn}})^{-1/2}$  (Sari et al. 1998). Similarly, the reverse-shock synchrotron flux at  $E^{\text{syn}} = 100$  keV lies in the energy range of  $E_{m,r}^{\text{syn}} < E^{\text{syn}}$  (see eq. 9). Therefore, it can be written as  $F_{\nu,r} = F_{\text{max},r}^{\text{syn}} (E_{m,r}^{\text{syn}}/E_{c,r}^{\text{syn}})^{-1/2} (E^{\text{syn}}/E_{m,r}^{\text{syn}})^{-p/2}$  (Sari et al. 1998). Using the values reported in equations (8) and (9), the synchrotron fluxes at forward and reverse shocks are  $F_{\nu,f} = 0.6$  mJy and  $F_{\nu,r} = 38.2$  mJy, respectively. The previous result indicates that synchrotron emission from the reverse shock is dominant over that radiation originated at the forward shock.

The electron population submerged in an oriented magnetic field radiates by synchrotron emission. For a perfectly uniform magnetic field, the linear polarizations of the synchrotron emission defined by power laws with spectral indexes  $1/2$ ,  $(p-1)/2$  and  $p/2$  are  $\Pi_{\text{max}} \simeq 69\%$ ,  $\Pi_{\text{max}} = \frac{p+1}{p+3/2} \times 100\% \simeq 71\%$  and  $\Pi_{\text{max}} = \frac{p+2}{p+10/3} \times 100\% \simeq 76\%$ , for 2.2 respectively (see; Gruzinov & Waxman 1999; Granot & Königl 2003, for discussion). Taking into account the temporal and energy range of the polarized photons detected (Yonetoku et al. 2012), the synchrotron spectrum with the microphysical parameters found lies in the fast-cooling regime and then,

the maximum polarization degree is 69%. Following Granot (2003) for a jet with an opening angle  $1/\Gamma \ll \theta$ , the ordered transverse magnetic field originated at the afterglow phase can give rise in principle to observed a polarization degree as high as  $\Pi_{\text{ord}} \simeq 58\%$  while the position angle does not vary significantly. This result is in agreement with the level of polarization degree and position angle observed by the GAP instrument. Therefore, polarization properties of the early reverse shock could explain the early observations reported in Yonetoku et al. (2012).

#### 4.3. Origin of the subdominant prompt thermal component

Since the subdominant prompt thermal component and the LAT light curve are present at the onset of this burst (Axelsson & et al. 2012), the main mechanisms discussed in the literature are revisited in order to interpret this subdominant prompt thermal component. These mechanisms are: the shock break out, the hot cocoon, the synchrotron external-shock self-absorption regime and the jet photosphere.

##### 4.3.1. The Shock Breakout

Shock breakout is the interpretation given to a short X-ray burst observed from a supernova. Shock breakouts are characterized by peak X-ray luminosities between  $10^{44} - 10^{46}$  erg/s (Campana & et al. 2006; Ensmann & Burrows 1992). Since this mechanism produces a thermal emission with very low luminosity, it is not consistent with the X-ray high luminosity detected in GRB 110721A.

##### 4.3.2. The Hot Cocoon

An alternative mechanism to explain the origin for thermal emission is the hot cocoon surrounding the jet. Pe'er et al. (2006) showed that a few hundred-seconds after the main emission, the cocoon emission lies in the X-ray band and the typical radii for the emission is larger than  $\geq 10^{12}$  cm. Using a relativistic expanding hot plasma cocoon, Starling et al. (2012) explained more than six bursts with black-body (BB) luminosities in the range of  $10^{47}$  to  $10^{49}$  erg/s when these emissions occurred during the steep decay phase of the X-ray light curve. They could not find any strong correlation between the BB properties and the prompt emission. Recently, a hydrodynamic simulations of the hot cocoon produced when a relativistic jet goes through the progenitor star was presented by De Colle et al. (2017). Authors reported an isotropic cocoon luminosity of  $\sim 10^{47}$  erg s $^{-1}$  which could be related with the X-ray luminosity detected during the plateau phase in a typical long-GRB afterglow. Due to the typical values of BB luminosities and the delay times between the prompt emission/early afterglow and the thermal emission, this model cannot explain the BB luminosity and the delay time observed in GRB 110721A.

##### 4.3.3. The Synchrotron External-shock Self-absorption Regime

Other mechanism that could describe the origin of the thermal component is the synchrotron external-shock spectrum in the strong self-absorption regime (Kobayashi et al. 2004; Gao et al. 2013). In the strong absorption regime, the synchrotron self-absorption energy ( $E_a^{\text{syn}}$ ) is larger than synchrotron cooling energy ( $E_c^{\text{syn}}$ ) and then, a thermal component due to pile-up of electrons would appear modifying the broken power-law spectrum. Otherwise, the synchrotron spectrum in the weak-absorption regime ( $E_a^{\text{syn}} < E_c^{\text{syn}}$ ) is not altered by the self-absorption process.

Using the observable quantities of GRB 110721A and requiring the microphysical parameter values found, the synchrotron self-absorption energies using  $z=3.512$  for forward and reverse shocks are

$$E_{a,f}^{\text{syn}} \simeq 1.1 \times 10^{-3} \text{ eV} \left( \frac{1+z}{4.512} \right)^{-2/5} \xi_{-0.12}^{-6/5} \epsilon_{e,-0.4}^{-1} \epsilon_{B,f,-5}^{1/5} \times A_{*, -1}^{6/5} E_{54.7}^{-2/5} t_{-0.5}^{-3/5} \quad (10)$$

and

$$E_{a,r}^{\text{syn}} \simeq 3.5 \times 10^{-10} \text{ eV} \left( \frac{1+z}{4.512} \right)^{-7/5} \xi_{-0.12}^{4/5} \epsilon_{e,-0.4}^{-1} \times \epsilon_{B,r,-0.4}^{1/5} \Gamma_3^2 A_{*, -1}^{11/5} E_{54.7}^{-7/5} t_{d,-0.5}^{2/5} \quad (11)$$

respectively. By comparing the equations (8) - (11), it can be seen that the self-absorption energies from the forward and reverse shocks lie in the weak-absorption regime, thus discarding this mechanism as possible origin of the subdominant prompt thermal component.

#### 4.3.4. The Jet Photosphere

The thermal photospheric component is related with the optically thick plasma of a relativistic jet (Guiriec et al. 2011, 2013, 2015). The thermal emission from the photosphere emerges when the optical depth of this fireball plasma becomes unity. Friis & Watson (2013) presented a search for thermal emission in the early X-ray afterglows. They identified a thermal component in eight bursts, determining very large luminosities ( $10^{48}$  to  $10^{52}$  erg/s), photospheric radii ( $\sim 10^{13}$  -  $10^{15.5}$  cm) and temperatures for many of them. They proposed that the thermal component in coincidence with the early  $\gamma$ -ray /X-ray afterglow could be modelled as late photospheric emission from the jet. They even claimed that this model could account for the thermal component present in GRB 110721A. Iyyani et al. (2013) studied GRB 110721A in the framework of photospheric emission. They found that the bulk Lorentz factor decreases monotonically with time from  $\sim 1000$  to  $\sim 150$ . Assuming a black hole mass of  $10 M_{\odot}$ , authors found that jet was moderately magnetized with a magnetization parameter of  $\sigma \sim 0.8$ .

If the dissipative effects below the photosphere take place (e.g. magnetic reconnection, shocks, etc), a copious pair formation dominates the photospheric opacity. In this case, the pair production induces a new photosphere farther out than the common baryonic photosphere, thus delaying the thermal emission (Rees & Mészáros 2005; Zhang & Yan 2011).

Pe'er (2008) showed that the photospheric radius strongly depends on the angle to the line of site. Thermal emission can be observed as long as tens of seconds following the decline of the central engine. Observation of the thermal emission at early times when it is observed along the line of site provides an unequivocal measurement of the temperature and photon flux. Otherwise, thermal emission detected at late times when the emission is off-axis could be observed and then could be relevant in the early afterglow phase, similar to the high-latitude emission discussed in the context of GRB afterglow (Fenimore et al. 1996; Kumar & Panaitescu 2000).

Considering that X-ray high luminosity of the subdominant prompt thermal component can be overlapped with the early afterglow phase, and also the values obtained in the early-afterglow external shock model similar to those

reported by Iyyani et al. (2013): i) The jet moderately magnetized with a value of magnetization parameter  $\sigma \sim 0.3-0.5$  and ii) the decrease of the value of bulk Lorentz factor  $\Gamma \sim 1000$ , therefore the subdominant prompt thermal component detected in GRB 110721A favors the late photospheric emission.

## 5. CONCLUSIONS

Analyzing the LAT data around the reported position of GRB 110721A with the most recent software SICENCE-TOOLS version v10r0p5 and reprocessing them with ‘‘Pass 8’’ extended, spacecraft data and the instrument response functions P8R2\_TRANSIENT020\_V6, the LAT light curve above 100 MeV and the photon index of GRB 110721A is reported. The LAT light curve presents a short-lived component peaking at  $\sim 0.25$  -  $0.35$  s and also a long-lived emission lasting hundreds of seconds. We have proposed that this light curve can have as origin those radiative processes generated in external shocks; the long-lived component by synchrotron radiation from forward shock and the short-lived emission by SSC emission from reverse shock. Additionally, we have found that the propagating outflow into a stellar wind evolved in the thick-shell case and must be moderately magnetized. The early high-energy photons ( $>100$  MeV) detected by LAT support the idea that these have as origin the external-shock region instead of internal-shock region as have been claimed by some authors (Maxham et al. 2011; He et al. 2011; Liu & Wang 2011).

We discuss the origin and the implications of the early-afterglow external shock model on the polarization observations, the extreme peak energy at  $15 \pm 2$  MeV and the subdominant prompt thermal component.

1. Based on the fact that photospheric and internal shock emission can hardly reproduce the high degree of linear polarization with a stable position angle and the LAT emission described in the early afterglow model, we show that reverse shock could explain the polarization properties observed in this burst. Using the condition of an opening angle  $1/\Gamma \ll \theta$  for the jet (Granot 2003), the ordered transverse magnetic field originated at the afterglow phase could in principle give rise to a polarization degree as high as  $\Pi_{\text{ord}} \simeq 58\%$  while the position angle does not vary significantly, as observed in GRB 110721A. It is worth noting that with the microphysical parameters found after describing the LAT emission, the synchrotron emission obtained from the reverse-shock region is dominant over the synchrotron flux from the forward shock.
2. Taking into account the peak exhibited in the LAT emission as the beginning of the deceleration of the jet, and the values of the magnetization parameters found after fitting the LAT light curve, it can be seen that the most suitable process to describe the extreme energy peak at  $15 \pm 2$  is the ICMART model (Zhang & Yan 2011). Studying the magnetization degree in the jet, and the evolution and the spectral features of the extreme peak energy, Zhang et al. (2012), Iyyani et al. (2013) and Gao & Zhang (2015) similarly found that the best candidate to explain this atypical peak was the ICMART process.
3. Several mechanisms were discussed in order to interpret the subdominant prompt thermal component. Taking into consideration the degree of magnetization and

the decreased value of bulk Lorentz factor as found after modeling the LAT emission and also the high luminosity of this thermal component, the late photospheric emission model is favored to describe the subdominant prompt thermal component.

The early-afterglow model used to describe the multiwavelength observations in GRB 110721A suggests that outflow is moderately magnetised  $\sigma \sim 0.3 - 0.5$ . This value is consistent with the fact that the reverse shock is strong and then the short-lived LAT emission could be successfully described (Zhang & Kobayashi 2005). A similar value of magnetization degree ( $\sigma \sim 0.8$ ) was found by Iyyani et al. (2013) after describing the thermal photospheric data. This magnetization is possible provided that the magnetic acceleration is inefficient (e.g. see, Veres et al. 2012).

Regarding that the ejecta propagating into the stellar wind is quickly decelerated, at  $\sim 0.3$  s, and using the typical value of stellar wind density of  $A = (5.0 \times 10^{10})$  g/cm (Chevalier & Li 2000; Ackermann et al. 2014; Ackermann & et al. 2013; Fraija et al. 2016a; Fraija 2015), then the bulk Lorentz fac-

tor is about  $\Gamma \sim 1000$  (Veres & Mészáros 2012; Ackermann & et al. 2013; Ackermann et al. 2014). This value is equal to that found by Iyyani et al. (2013) after describing the subdominant prompt thermal data as photospheric emission.

The early-afterglow external shock model proposed to explain the high-energy emission in GRB110721A indicates that the outflow carries a meaningful magnetic field. Similar results have been found in the most luminous LAT-detected bursts such as GRB090902B (Abdo et al. 2009), GRB110731A (Ackermann & et al. 2013; Fraija 2015), GRB130427A (Ackermann et al. 2014; Fraija et al. 2016a), GRB160625B (Zhang et al. 2016; Fraija et al. 2017), among others. What makes it unique is the large amount of Poynting flux that must have been dissipated during the prompt emission phase.

#### ACKNOWLEDGEMENTS

We thank Dimitrios Giannios, Fabio de Colle, Bing Zhang, Anatoly Spitovskiy and Simone Dichiara for useful discussions. NF acknowledges financial support from UNAM-DGAPA-PAPIIT through grant IA102917 and WHL through grant 100317. PV thanks Fermi grant NNM11AA01A and partial support from OTKA NN 111016 grant.

#### REFERENCES

- Abdo, A. A., Ackermann, M., Ajello, M., et al. 2009, *ApJ*, 706, L138  
 Ackermann, M., & et al. 2010, *ApJ*, 716, 1178  
 —. 2013, *ApJ*, 763, 71  
 Ackermann, M., Ajello, M., Asano, K., et al. 2013, *ApJS*, 209, 11  
 —. 2014, *Science*, 343, 42  
 Ahlgren, B., Larsson, J., Nymark, T., Ryde, F., & Pe'er, A. 2015, *MNRAS*, 454, L31  
 Amati, L., Guidorzi, C., Frontera, F., et al. 2008, *MNRAS*, 391, 577  
 Arnaud, K. A. 1996, in *Astronomical Society of the Pacific Conference Series*, Vol. 101, *Astronomical Data Analysis Software and Systems V*, ed. G. H. Jacoby & J. Barnes, 17  
 Axelsson, M., & et al. 2012, *ApJ*, 757, L31  
 Bégué, D., & Pe'er, A. 2015, *ApJ*, 802, 134  
 Beniamini, P., Nava, L., Duran, R. B., & Piran, T. 2015, *MNRAS*, 454, 1073  
 Beniamini, P., & Piran, T. 2013, *ApJ*, 769, 69  
 Berger, E. 2011, *GRB Coordinates Network*, 12193, 1  
 Blandford, R. D., & Znajek, R. L. 1977, *MNRAS*, 179, 433  
 Bromberg, O., & Tchekhovskoy, A. 2016, *MNRAS*, 456, 1739  
 Brun, R., & Rademakers, F. 1997, *Nuclear Instruments and Methods in Physics Research A*, 389, 81  
 Campana, S., & et al. 2006, *Nature*, 442, 1008  
 Chevalier, R. A., & Li, Z.-Y. 2000, *ApJ*, 536, 195  
 Coburn, W., & Boggs, S. E. 2003, *Nature*, 423, 415  
 Corsi, A., Guetta, D., & Piro, L. 2010, *ApJ*, 720, 1008  
 Covino, S., Lazzati, D., Ghisellini, G., et al. 1999, *A&A*, 348, L1  
 De Colle, F., Lu, W., Kumar, P., Ramirez-Ruiz, E., & Smoot, G. 2017, *ArXiv e-prints*, arXiv:1701.05198  
 Ensman, L., & Burrows, A. 1992, *ApJ*, 393, 742  
 Fan, Y. Z., Wei, D. M., & Wang, C. F. 2004, *A&A*, 424, 477  
 Fan, Y.-Z., Tam, P. H. T., Zhang, F.-W., et al. 2013, *ApJ*, 776, 95  
 Fenimore, E. E., Madras, C. D., & Nayakshin, S. 1996, *ApJ*, 473, 998  
 Fraija, N. 2015, *ApJ*, 804, 105  
 Fraija, N., González, M. M., & Lee, W. H. 2012, *ApJ*, 751, 33  
 Fraija, N., Lee, W., & Veres, P. 2016a, *ApJ*, 818, 190  
 Fraija, N., Lee, W. H., Veres, P., & Barniol Duran, R. 2016b, *ApJ*, 831, 22  
 Fraija, N., Veres, P., Zhang, B. B., et al. 2017, *ArXiv e-prints*, arXiv:1705.09311  
 Friis, M., & Watson, D. 2013, *ApJ*, 771, 15  
 Gao, H., Lei, W.-H., Wu, X.-F., & Zhang, B. 2013, *MNRAS*, 435, 2520  
 Gao, H., & Zhang, B. 2015, *ApJ*, 801, 103  
 Ghisellini, G., Ghirlanda, G., Nava, L., & Celotti, A. 2010, *MNRAS*, 403, 926  
 Gorbvskoy, E. S., Lipunov, V. M., Buckley, D. A. H., et al. 2016, *MNRAS*, 455, 3312  
 Götz, D., Laurent, P., Lebrun, F., Daigne, F., & Bošnjak, Ž. 2009, *ApJ*, 695, L208  
 Granot, J. 2003, *ApJ*, 596, L17  
 Granot, J., & Königl, A. 2003, *ApJ*, 594, L83  
 Granot, J., Piran, T., Bromberg, O., Racusin, J. L., & Daigne, F. 2015, *Space Sci. Rev.*, 191, 471  
 Greiner, J., Utdike, A. C., Kruehler, T., & Sudilovsky, V. 2011, *GRB Coordinates Network*, 12192, 1  
 Greiner, J., Klose, S., Reinsch, K., et al. 2003, *Nature*, 426, 157  
 Grupe, D., Swenson, C. A., Racusin, J. L., & Wolf, C. 2011, *GRB Coordinates Network*, 12212, 1  
 Gruzinov, A., & Waxman, E. 1999, *ApJ*, 511, 852  
 Guetta, D., Spada, M., & Waxman, E. 2001, *ApJ*, 557, 399  
 Guiriec, S., Mochkovitch, R., Piran, T., et al. 2015, *ApJ*, 814, 10  
 Guiriec, S., Connaughton, V., Briggs, M. S., et al. 2011, *ApJ*, 727, L33  
 Guiriec, S., Daigne, F., Hascoët, R., et al. 2013, *ApJ*, 770, 32  
 He, H.-N., Wu, X.-F., Toma, K., Wang, X.-Y., & Mészáros, P. 2011, *ApJ*, 733, 22  
 Inoue, T., Asano, K., & Ioka, K. 2011, *ApJ*, 734, 77  
 Iyyani, S., Ryde, F., Burgess, J. M., Pe'er, A., & Bégué, D. 2016, *MNRAS*, 456, 2157  
 Iyyani, S., Ryde, F., Axelsson, M., et al. 2013, *MNRAS*, 433, 2739  
 Kobayashi, S., Mészáros, P., & Zhang, B. 2004, *ApJ*, 601, L13  
 Kobayashi, S., & Zhang, B. 2003, *ApJ*, 597, 455  
 —. 2007, *ApJ*, 655, 973  
 Kobayashi, S., Zhang, B., Mészáros, P., & Burrows, D. 2007, *ApJ*, 655, 391  
 Komissarov, S. S. 2001, *MNRAS*, 326, L41  
 Kopač, D., Mundell, C. G., Japelj, J., et al. 2015, *ApJ*, 813, 1  
 Kumar, P., & Barniol Duran, R. 2009, *MNRAS*, 400, L75  
 —. 2010, *MNRAS*, 409, 226  
 Kumar, P., & Panaitescu, A. 2000, *ApJ*, 541, L51  
 Liu, R.-Y., & Wang, X.-Y. 2011, *ApJ*, 730, 1  
 Lundman, C., Pe'er, A., & Ryde, F. 2013, *MNRAS*, 428, 2430  
 Maxham, A., Zhang, B.-B., & Zhang, B. 2011, *MNRAS*, 415, 77  
 Mundell, C. G., Steele, I. A., Smith, R. J., et al. 2007, *Science*, 315, 1822  
 Mundell, C. G., Kopač, D., Arnold, D. M., et al. 2013, *Nature*, 504, 119  
 Panaitescu, A., & Mészáros, P. 1998, *ApJ*, 493, L31  
 Pe'er, A. 2008, *ApJ*, 682, 463  
 Pe'er, A., Barlow, H., O'Mahony, S., et al. 2015, *ApJ*, 813, 127  
 Pe'er, A., Mészáros, P., & Rees, M. J. 2006, *ApJ*, 652, 482  
 Piran, T. 1999, *Phys. Rep.*, 314, 575  
 Piran, T. 2005, in *American Institute of Physics Conference Series*, Vol. 784, *Magnetic Fields in the Universe: From Laboratory and Stars to Primordial Structures*, ed. E. M. de Gouveia dal Pino, G. Lugones, & A. Lazarian, 164–174  
 Pruzhinskaya, M. V., Krushinsky, V. V., Lipunova, G. V., et al. 2014, *New A*, 29, 65  
 Rees, M. J., & Meszaros, P. 1994, *ApJ*, 430, L93  
 Rees, M. J., & Mészáros, P. 2005, *ApJ*, 628, 847  
 Rutledge, R. E., & Fox, D. B. 2004, *MNRAS*, 350, 1288  
 Rybicki, G. B., & Lightman, A. P. 1986, *Radiative Processes in Astrophysics*

- Sacahui, J. R., Fraija, N., González, M. M., & Lee, W. H. 2012, *ApJ*, 755, 127
- Sari, R., Piran, T., & Narayan, R. 1998, *ApJ*, 497, L17
- Spergel, D. N., Verde, L., Peiris, H. V., et al. 2003, *ApJS*, 148, 175
- Starling, R. L. C., Page, K. L., Pe’Er, A., Beardmore, A. P., & Osborne, J. P. 2012, *MNRAS*, 427, 2950
- Steele, I. A., Mundell, C. G., Smith, R. J., Kobayashi, S., & Guidorzi, C. 2009, *Nature*, 462, 767
- Tchekhovskoy, A. 2015, in *Astrophysics and Space Science Library*, Vol. 414, *The Formation and Disruption of Black Hole Jets*, ed. I. Contopoulos, D. Gabuzda, & N. Kylafis, 45
- Tchekhovskoy, A., Narayan, R., & McKinney, J. C. 2010, *ApJ*, 711, 50
- Tierney, D., & von Kienlin, A. 2011, *GRB Coordinates Network*, 12187
- Uhm, Z. L., & Zhang, B. 2014, *Nature Physics*, 10, 351
- Vasileiou, V., Piron, F., Tierney, D., et al. 2011, *GRB Coordinates Network*, 12188
- Veres, P., & Mészáros, P. 2012, *ApJ*, 755, 12
- Veres, P., Zhang, B.-B., & Mészáros, P. 2012, *ApJ*, 761, L18
- Virgili, F., Japelj, J., & Guidorzi, C. 2012, *GRB Coordinates Network*, 13018
- Yonetoku, D., Murakami, T., Gunji, S., et al. 2011, *ApJ*, 743, L30
- . 2012, *ApJ*, 758, L1
- Zhang, B., & Kobayashi, S. 2005, *ApJ*, 628, 315
- Zhang, B., Kobayashi, S., & Mészáros, P. 2003, *ApJ*, 595, 950
- Zhang, B., Lu, R.-J., Liang, E.-W., & Wu, X.-F. 2012, *ApJ*, 758, L34
- Zhang, B., & Yan, H. 2011, *ApJ*, 726, 90
- Zhang, B.-B., Zhang, B., Castro-Tirado, A. J., et al. 2016, *ArXiv e-prints*, arXiv:1612.03089

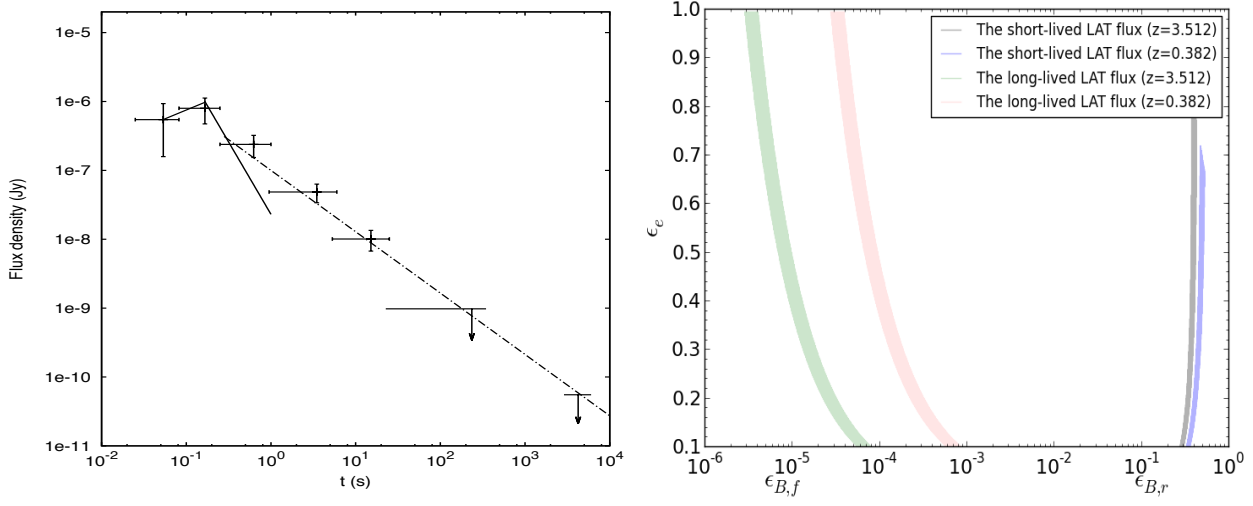


FIG. 1.— Left panel corresponds to the fit of the LAT light curve (above 100 MeV) of GRB 110721A observation with the early-afterglow external-shock model (Fraija 2015; Fraija et al. 2016a). We use the reverse shock in the thick-shell regime to describe the short-lived component (solid line) and the forward shock to explain the long-lived component (dash-dotted line). For this fit we have used the values of  $E_{\gamma,\text{iso}} = 1.4 \times 10^{52}$  erg and  $E_{\gamma,\text{iso}} = 1.2 \times 10^{54}$  erg for  $z=0.382$  and  $z=3.512$ , respectively, and the values of microphysical parameters obtained in each case are shown in the right panel. This panel shows the values of the microphysical parameters ( $\epsilon_e$ ,  $\epsilon_{B,f}$  and  $\epsilon_{B,r}$ ), that explain the LAT light curve for  $z=0.382$  and  $z=3.512$ . The parameter region at the left side in this panel reproduces the long-lived LAT flux through synchrotron emission from forward shock and at the right side describes the short-lived LAT flux by SSC from reverse shock.